Measurement: Sensors 15 (2021) 100042

Contents lists available at ScienceDirect

Measurement: Sensors

journal homepage: www.journals.elsevier.com/measurement

Customized piezoresistive microprobes for combined imaging of topography and mechanical properties

Michael Fahrbach [a,b,*], Sebastian Friedrich [c], Heinrich Behle [d], Min Xu [d], Brunero Cappella [c], Uwe Brand [d], Erwin Peiner [a,b]

[a] Technische Universität Braunschweig, Institute of Semiconductor Technology (IHT), Hans-Sommer-Straβe 66, 38106, Braunschweig, Germany
[b] Laboratory for Emerging Nanometrology (LENA), Langer Kamp 6 a/b, 38106, Braunschweig, Germany
[c] Federal Institute for Material Research and Testing (BAM), Unter den Eichen 87, 12205, Berlin, Germany
[d] Physikalisch-Technische Bundesanstalt (PTB), Bundesallee 100, 38116, Braunschweig, Germany

ARTICLE INFO

Keywords:
Cantilever microprobe
Piezoresistive
Atomic force microscopy
Force–distance curves
Contact resonance
Lubricants

ABSTRACT

Customized piezoresistive cantilever microprobes with a deflection range of 120 μm and silicon tips of 100 μm height were operated in a Cypher AFM showing their functionality for measuring topography together with viscoelastic properties of thin films. For drop-in mounting in the AFM a holder was developed comprising the piezoresistive microprobe and its voltage-supply and signal-conditioning electronics. With the probe tip in contact to a glass sample we found a vertical resolution of 2.8 nm in a bandwidth of 1 kHz, which is close to the theoretical limit of 3.0 nm at a deflection of 2.5 μm. This resolution could be verified in topographic images of a scratch of approximately 300 nm in depth. Force-volume images with lithographically patterned photoresist (AZ 5214E) of approximately 300 nm thickness on silicon revealed contrast of the resist-covered and bare regions in topography, stiffness and adhesion. With contact-resonance imaging using the Dual AC Resonance Tracking (DART) method, patterned AZ 5214E photoresist of approximately 50 nm thickness could be distinguished from the bare silicon in topography, contact stiffness (indicated by contact resonance frequency shift) and adhesion (indicated by phase shift). Finally, a droplet of lubricant (Lupranol VP 9209) on glass could be detected by force volume imaging revealing a thickness of approximately 90 nm of the liquid layer with a sharp lateral limitation, which was clearly detected. We conclude that the piezoresistive silicon microprobe is a promising tool for emerging tasks of industrial surface metrology on manufacturing machines, including micro-finish of work pieces and elasticity, thickness, adhesion, etc. of thin solid or liquid deposits on top.

1. Introduction

Piezoresistive microprobes with specifically designed dimensions and shape allow to measure samples with geometrical constraints that prevent an application of the optical lever technique. As an example, we showed the use of extremely slender cantilevers (length 1.5 mm, width 30 μm and height 25 μm) for inner surface characterization of fuel injector nozzle spray holes. These holes have diameters down to 100 μm and depths of a millimeter [1,2]. Using even larger microprobes (length 5 mm, width 200 μm and height 50 μm, CAN50-2-5, CiS Forschungsinstitut für Mikrosensorik GmbH, Erfurt, Germany [3,4]), fast scanning of technical work piece surfaces containing high-aspect-ratio microstructures is feasible for roughness measurements at speeds up to 15 mm/s [5]. Based on these findings a battery-operated hand-held miniature roughness tester with an integrated skid body was developed. This device uses a microprobe with a very short measurement loop to measure autonomously inside bores of 6 mm in diameter while the data is transmitted to a computer via Bluetooth [6]. The european EMPIR project MicroProbes currently investigates to use these sensors to monitor both the quality of polished gears and the result of roll-grinding processes. Furthermore, evaluations of the progress of scratch damage in ceramics are being carried out [7]. Additionally, topography measurement with such piezoresistive microprobes was combined with a characterization of viscoelastic properties of thin surface deposits using contact resonance spectroscopy [6,8,9].

For characterizing the microprobe's large deflection range, e. g., within 70 μm of z displacement showing a standard deviation of

* Corresponding author. Technische Universität Braunschweig, Institute of Semiconductor Technology (IHT), Hans-Sommer-Straβe 66, 38106, Braunschweig, Germany.
E-mail address: m.fahrbach@tu-bs.de (M. Fahrbach).

https://doi.org/10.1016/j.measen.2021.100042
Received 30 September 2020; Received in revised form 16 February 2021; Accepted 3 March 2021
Available online 17 March 2021

approximately 30 nm_{rms} [9] either a homemade setup or the Profilscanner of PTB was employed [10–12]. In this study, we further investigate the performance and limitations of the CAN50-2-5 microprobes at the lower end of their measuring range with the help of the imaging versatility of a commercial atomic force microscope (AFM, Cypher, Asylum Research, Oxford Instruments, Santa Barbara, USA). For this, the design and fabrication of an adapted probe holder was necessary. The performance of the CAN50-2-5 microprobes could then be investigated and compared to standard Nanosensors PPP-NCSTAuD AFM probes (NanoWorld, Neuchatel, Switzerland), which are operated in the Cypher AFM using the conventional optical lever technique.

Piezoresistive cantilevers for atomic force microscopy (AFM) have been in use for decades and are commercially available, e. g., from SCL-Sensor.Tech. Fabrication GmbH, Austria. A big advantage over the standard optical-lever read out is a simplified calibration which is needed to be done only once instead of the necessary repeated recalibrations due to a not constant laser spot position on the cantilever between measurements. However, a custom-made holder is yet required for operation of such piezoresistive cantilevers in a commercial AFM [13]. Still, a custom holder allows to exploit the low-noise operating conditions of an AFM for testing the performance of various designs of piezoresistive cantilevers, e. g. the CAN50-2-5 microprobe with respect to its smallest detectable deflection, which is addressed in the following.

2. Microprobe

The basic structure of the CAN50-2-5 microprobes is shown in Fig. 1. It is made from silicon and consists of two parts: the base and the cantilever. A monolithic silicon probing tip, as shown in Fig. 2, is located near the free end of the cantilever and a piezoresistive Wheatstone bridge is implanted at the clamped end. The base contains the contact pads to connect to the bridge.

As shown in Fig. 3, deflecting the probing tip results in a linear change of the amplified output voltage of the Wheatstone bridge. In this measurement, a resolution of approx. 30 nm_{rms} for all deflections up to 120 µm and a non-linearity of approx. 0.4 % is achieved. This is in line with previous publications, where a non-linearity of 0.3 % at deflections up to 200 µm was reported [3,4,14,15].

3. Microprobe holder

The original cantilever holder of the AFM (Cypher 901.705 Invar Air Cantilever Holder), which is shown in Fig. 4, cannot be used with customized piezoresistive microprobes like the CAN50-2-5. For this reason, an adapted probe holder as well as electronics to interface the piezoresistive microprobe with the microscope had to be developed.

The new holder for the CAN50-2-5 comprises an aluminum body as well as PCBs for the microprobe attach and the interface to the AFM, respectively. It was designed as a drop-in replacement and does not require any changes to be made to the microscope. The interface PCB is supplied with power by the AFM (+12 V, 0 V, −12 V and 3.3 V) and generates a stabilized supply voltage of 1 V for the piezoresistive Wheatstone bridge of the microprobe. In the reverse direction it amplifies the output signal of the microprobe and feeds it into the Cypher electronics.

Fig. 5 shows in a transport box the adapted holder for the CAN50-2-5 with the aluminum body whereon the two PCBs (interface PCB and microprobe PCB) are screwed in place. The microprobe PCB is used as substrate for attach and electrical contact of the microprobe chip. The

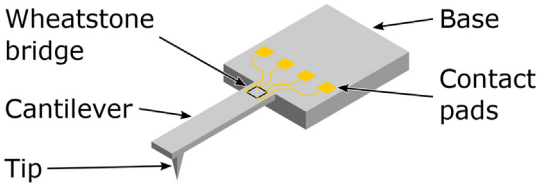

Fig. 1. Schematic of the piezoresistive microprobe.

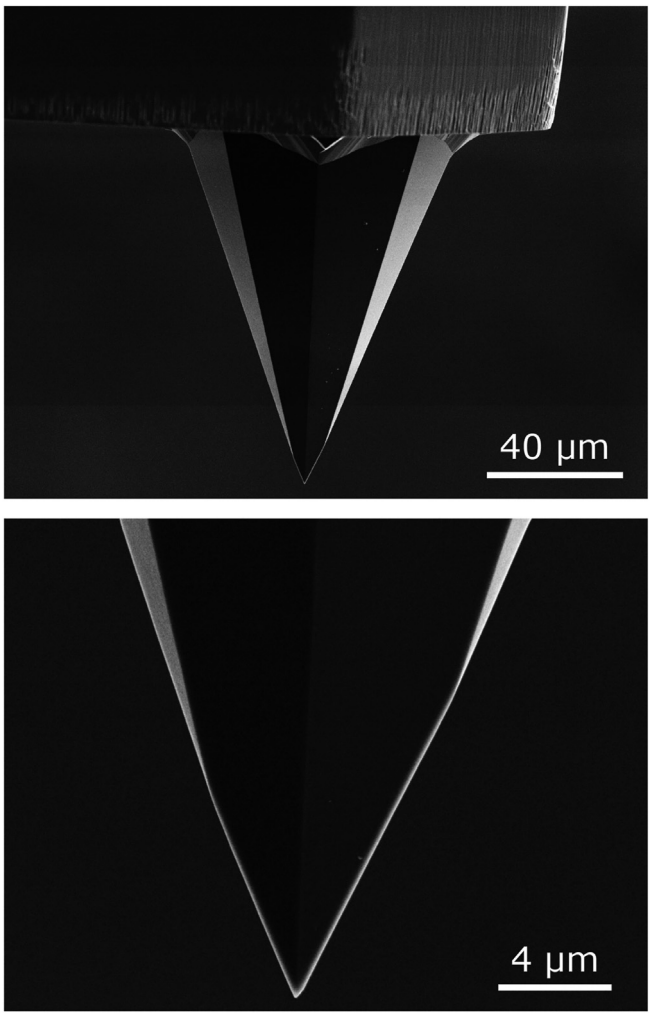

Fig. 2. Scanning electron microscopy (SEM) images of the probing tip used in this study. **(Top)** overview of the tip and **(bottom)** close-up of the apex. The images were taken before any measurements were conducted. The tip height, radius and cone angle approximately are 100 µm, 70 nm and 45°–50°, respectively. The mass of the tip (≈ 0.4 µg) can be neglected in relation to the mass of the cantilever (≈ 120 µg).

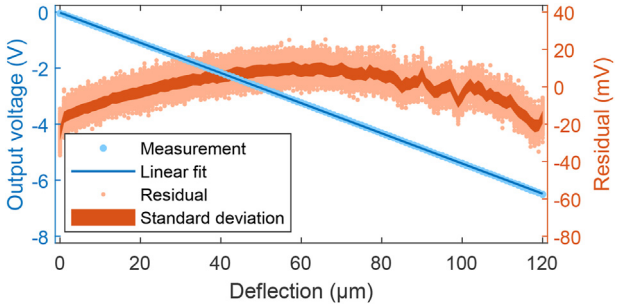

Fig. 3. Quasi-static voltage-displacement curve of a CAN50-2-5 microprobe measured using the Profilscanner of PTB [10–12]. The maximum deflection was limited by the dynamic range of the amplifier. Measured values are shown as light blue dots, a linear fit with a slope of 53.8 mV/µm is shown as a dark blue line. The residuals with standard deviations are shown as light red dots with a dark red area. (For interpretation of the references to colour in this figure legend, the reader is referred to the Web version of this article.)

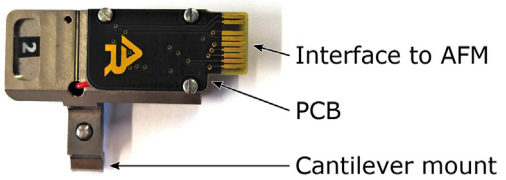

Fig. 4. Original Cypher holder and PCB for mounting of AFM cantilevers within the instrument.

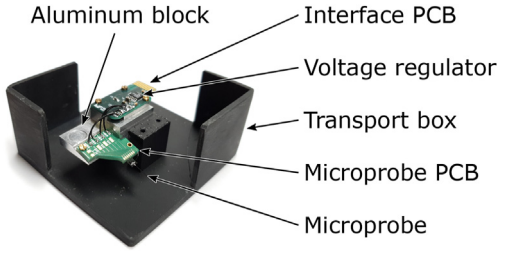

Fig. 5. Developed microprobe holder (in a transport box) comprising an aluminium body and two PCBs to operate long slender piezoresistive CAN50-2-5 microprobes in the Cypher AFM.

interface PCB contains all electronic components. This includes a voltage regulator (LT3045, Analog Devices) to generate the stabilized supply voltage for the microprobe and an instrumentation pre-amplifier (AD8421, Analog Devices) to amplify (gain = 100) and buffer the output signal. Finally, the amplified signal is fed to one of the so-called *holder input* channels of the AFM. Here it is available at the *Cypher Crosspoint switch* and can be connected to the ADC. The control unit of the AFM will then use this signal alternately with the cantilever-deflection amplitude provided by the quadrant photo diode of the optical lever system.

The attach of the microprobe die to its PCB is done by gluing (UHU Plus Endfest, UHU GmbH & Co. KG, Germany) and electrical connection via wire bonding (AlSi wire, 25 µm, ultrasonic bonding (Model 7476E, West·Bond, Inc., USA)). To ensure force closure, the microprobe PCB is glued to the aluminum block as well. Both PCBs are electrically connected via soldered copper wires.

3.1. Resolution considerations

To estimate the performance of the microprobe setup, first the noise of the output signal is estimated. For this purpose, the parameters defined in Table 1 are used in combination with Equations (1)–(5) to obtain estimates of the sensitivity, noise and resolution of our piezoresistive microprobe. In general, for piezoresistive silicon sensors, the following contributions to noise have to be considered:

3.1.1. Mechanical-thermal noise of the cantilever $\overline{\delta^2_{m-th}}$

With the cantilever considered as a spring-mass resonator in the accelerometer limit ($f \ll f_0$), mechanical-thermal noise is given by Ref. [16]:

$$\overline{\delta^2_{\mathrm{m-th}}} = \frac{8\pi k_B T}{k_c Q f_0}\Delta f = (0.492\ \ \mathrm{fm_{RMS}})^2. \tag{1}$$

Here, k_B is Boltzmann's constant and Δf is the bandwidth. T and k_c are the temperature and spring constant (also known as the elastic constant) of the microprobe, respectively. Q and f_0 are the quality factor and the resonance frequency of the fundamental vibration mode of the probe, respectively.

Table 1
Mechanical, geometrical and electrical parameters that are used to estimate the noise floor of the microprobe-based measurement system.

Parameter	Symbol	Value
Measurement		
Frequency range minimum	$f_{\min}$	0.001 Hz
Frequency range maximum	$f_{\max}$	1000 Hz
Bandwidth	$\Delta f = f_{\max} - f_{\min}$	999.999 Hz
Ambient Temperature	T	293 K
Cantilever		
Young's modulus	E	169 GPa [18]
Density	ρ	2330 $\mathrm{kg/m^3}$
Length	L	5 mm [4]
Width	w	200 µm [4]
Thickness	b	50 µm [4]
Area moment of inertia	$I = \frac{wb^3}{12}$	2.093×10^{-18} $\mathrm{m^4}$
Spring constant [19]	$k_c \approx \frac{Eb^3 w}{4L^3}$	8.45 N/m
Doping concentration	ρ	$(2.25 \pm 0.75) \times 10^{18}$ $\mathrm{cm^{-3}}$ [15]
Piezoresistive coefficient	$\pi_{44} = P(p,T) \times \pi_{44}^{\mathrm{ref}}$	$(1.07 \pm 0.05)\mathrm{GPa^{-1}}$ [17]
Longitudinal piezoresistive coefficient	$\pi_{\mathrm{eff}} \approx \frac{\pi_{44}}{2}$	$(0.54 \pm 0.03)\mathrm{GPa^{-1}}$
Sensitivity, theoretical [17]	$S \approx \frac{6\pi_{\mathrm{eff}} L k_c U_0}{wb^2}$	271 V/m
Sensitivity, measured	S_{meas}	252 V/m
Hooge constant per number of carriers	$\frac{\alpha_H}{N}$	5.6×10^{-14} [20]
Bridge resistance	R	2.5 kΩ[4]
Fundamental mode wavenumber	$x_0 L$	1.87510 [19]
Fundamental mode resonance frequency [19]	$f_0 = \frac{(x_0 L)^2}{2\pi L^2}\sqrt{\frac{EI}{\rho w b}}$	2751.5 Hz
Fundamental mode quality factor	Q	430 [6]
$1/f$ noise spectral density, voltage	V_{VF}	1 µV [21]
Voltage regulator		
$1/f$ noise exponent	β	1.5 [21]
Johnson noise spectral density, voltage	V_{VJ}	2 $\mathrm{nV/\sqrt{Hz}}$ [21,22]
Bridge supply voltage	U_0	1 V
Amplifier		
Johnson noise spectral density, voltage	A_{VJ}	3.31 $\mathrm{nV/\sqrt{Hz}}$ @ G = 100 [23]
Johnson noise spectral density, current	A_{IJ}	0.2 $\mathrm{pA/\sqrt{Hz}}$ [23]
$1/f$ noise, voltage	A_{VF}	7 nV @ $G = 100$ f = 1 Hz [23]
$1/f$ noise, current	A_{IF}	1.26 pA @ f = 0.1 Hz [23]

3.1.2. Electrical noise of the Wheatstone bridge $\overline{V^2_{N,Bridge}}$

Electrical noise comprises of $1/f$-noise and Nyquist Johnson noise. For the Wheatstone bridge, $1/f$-noise is calculated using the device specific Hooge constant α_H , the bridge supply voltage U_0, the number of carriers per resistor N, and the bandwidth given by $f_{\max}$ and $f_{\min}$. Nyquist-Johnson noise is calculated using Boltzmann's constant k_B , the temperature of the bridge T, the resistance of a single bridge resistor R, and the bandwidth Δf [17].

$$\overline{V^2_{\mathrm{N,Bridge}}} = \frac{\alpha_H U_0^2}{2N}\ln\left(\frac{f_{\max}}{f_{\min}}\right) + 4k_B T R \Delta f = (0.653\ \ \mu\mathrm{V_{RMS}})^2 \tag{2}$$

3.1.3. Electrical noise of the voltage regulator module $V^2_{N,VRM}$

The voltage regulator module, short VRM, provides the Wheatstone bridge supply voltage. For this device, the datasheet only specifies noise starting at 10 Hz [22]. Achtenberg et al. [21] measured the output noise spectrum down to 0.1 Hz and show $1/f$-noise decreasing with the

exponent $\beta \approx 1.5$. By extrapolating that behavior for lower frequencies, the integral noise can be calculated as

$$\overline{V^2_{\mathrm{N,VRM}}} \approx \frac{1}{2\beta-1} V^2_{\mathrm{VF}} f^{2\beta}_{\mathrm{V,VF}} \left(\frac{1}{f^{2\beta-1}_{\mathrm{min}}} - \frac{1}{f^{2\beta-1}_{\mathrm{max}}} \right) + V^2_{\mathrm{VJ}} \Delta f \approx (707\ \mu\mathrm{V_{RMS}})^2 \tag{3}$$

Here, V_{VF} is the spectral density of $1/f$ noise measured at the frequency $f_{\mathrm{V,VF}}$. V_{VJ} is the spectral density of Nyquist-Johnson noise.

The output noise of the voltage regulator only contributes to the total noise when the output voltage of the microprobe is greater than zero, i.e. when the cantilever is deflected. As such it can be neglected at small deflections (< 100 nm). Furthermore, this noise contribution mainly consists of $1/f$-noise, wherefore its impact is reduced drastically when decreasing measurement time. However, the microprobe is made to be used at large deflections up to 200 μm and for long measurement times, so this noise contribution must be considered.

3.1.4. Electrical noise of the preamplifier $\overline{V^2_{N,Amp}}$

The noise of the amplifier is given by the voltage and current components of $1/f$-noise (A_{VF} and A_{IF}) and Nyquist-Johnson noise (A_{VJ} and A_{IJ}), respectively [17].

$$\overline{V^2_{\mathrm{N,Amp}}} = \left(A^2_{\mathrm{VF}} + 2A^2_{\mathrm{IF}} \left[\frac{R}{2}\right] \right) \ln\left(\frac{f_{\mathrm{max}}}{f_{\mathrm{min}}}\right) + \left(A^2_{\mathrm{VJ}} + 2A^2_{\mathrm{IJ}} \left[\frac{R}{2}\right] \right) \Delta f = (0.109\ \mu\mathrm{V_{RMS}})^2 \tag{4}$$

3.1.5. Total input-referred noise of deflection $\sqrt{\overline{\delta^2_N}}$

Total noise limits the resolution that can be achieved and is calculated from the above non-correlated noise contributions according to:

$$\sqrt{\overline{\delta^2_{\mathrm{N}}}} = \frac{\sqrt{\overline{\delta^2_{\mathrm{m-th}}} + \frac{\overline{V^2_{\mathrm{N,VRM}}}}{U^2_0}\delta^2 + \overline{V^2_{\mathrm{N,Bridge}}} + \overline{V^2_{\mathrm{N,Amp}}}}}{S^2} = 3.0\ \ \mathrm{nm_{RMS}} \tag{5}$$

Here, δ is the typical deflection of the microprobe. At $\delta = 0$ we find $\sqrt{\overline{\delta^2_{\mathrm{N}}}} = 2.4\ \ \mathrm{nm_{RMS}}$. Above $\delta \approx 4$ μm, total noise is dominated by the $1/f$-noise of the voltage regulator and thus is expected to increase to $\sqrt{\overline{\delta^2_{\mathrm{N}}}} = 141\ \ \mathrm{nm_{RMS}}$ at the upper deflection-range limit of the microprobe of $\delta \approx 200$ μm. The contribution of the voltage-regulator noise can be considerably reduced by selecting a higher Wheatstone-bridge supply voltage. At a voltage of $U_0 = 2$ V, we expect noise of 2.3 $\mathrm{nm_{RMS}}$, 2.5 $\mathrm{nm_{RMS}}$, and 71 $\mathrm{nm_{RMS}}$ for deflections of 0 μm, 2.5 μm and 200 μm, respectively. However, this increases both power consumption and the time it takes for the probe to reach thermal equilibrium. Alternatively, lower noise can be expected if, instead of a voltage regulator, a constant voltage source is used to supply U_0. For example, the output of an LT6657 voltage reference with an output voltage of 1.25 V can achieve approximately 1 $\mu\mathrm{V_{RMS}}$ of noise within the required bandwidth [24]. This can be neglected in comparison to the other noise contributions and results in noise of 2.4 $\mathrm{nm_{RMS}}$ for all deflections up to 200 μm. However, in this case U_0 will be fixed and cannot be adjusted to changing measurement requirements.

The measured value of sensitivity S_{meas} of the CAN50-2-5 piezoresistive microprobe deviates from the theoretical expectation by −10.6 %, which can be assigned mainly to the cantilever thickness b, that can only be specified with an uncertainty up to ±2.2 % [15]. For the uncertainty of sensitivity an additional contribution due to the piezoresistive coefficient of ±6.3 % was assumed. Following the error propagation law this leads to uncertainties ±6.6 % in k_c and ±10.1 % in S, which explain the observed deviations.

Our detailed noise analysis yields a resolution, i. e., a minimum detectable tip deflection of the CAN50-2-5 piezoresistive microprobes of 3.0 nm in a bandwidth of 0.001 Hz to 1 kHz with deflections up to 2.5 μm. In the following we will present experimental results to verify this theoretical expectation.

It should be noted that commercial piezoresistive AFM cantilevers have much smaller dimensions leading to much higher sensitivity S and correspondingly lower minimum detectable tip deflections compared to the piezoresistive microprobe considered here. Assuming scaling factor of κ, i. e., $L_{\mathrm{AFM}} = \kappa \times L_{\mathrm{microprobe}}$ and $b_{\mathrm{AFM}} = \kappa \times b_{\mathrm{microprobe}}$, and using the respective Eqs. in Table 1 we can estimate $S_{\mathrm{AFM}} = \kappa^{-1} \times S_{\mathrm{microprobe}}$.

Furthermore, if the electrical noise of the Wheatstone bridge remains unchanged, total noise at small deflections is given by:

$$\sqrt{\overline{\delta^2_{\mathrm{N_{AFM}}}}} = \kappa \sqrt{\overline{\delta^2_{\mathrm{N_{microprobe}}}}}. \tag{6}$$

With piezoresistive AFM cantilevers of $L = 300$ μm, b = 4 μm to 6 μm (PRSA probes, SCL-Sensor. Tech. Fabrication GmbH, Austria) we approximate $\kappa \approx 0.1$ and obtain a sensitivity of $S \approx 3$ kV/m and a resolution of $\sqrt{\overline{\delta^2_{\mathrm{N_{AFM}}}}} \approx 0.1$ nm at $\Delta f = 1$ kHz, which was experimentally confirmed yielding $S \approx 4$ kV/m and $\sqrt{\overline{\delta^2_{\mathrm{N_{AFM}}}}} \approx 0.1$ nm using a piezoresistive pseudo half-bridge configuration of $R = 1$ kΩ and a longitudinal piezoresistive coefficient of $\pi_{\mathrm{eff}} = 0.472\ \ \mathrm{GPa^{-1}}$, operated at $U_0 = 2$ V in a bandwidth of $\Delta f = 4.8$ kHz [13].

4. Results

Measurements with the piezoresistive microprobes mounted in a Cypher AFM can be performed by exploiting either the laser signal via the common optical lever method [25, pp. 67–69] or the output signal of the piezoresistive microprobe. Unfortunately, these two signals cannot be acquired simultaneously.

Fig. 6 shows deflection-displacement curves on a glass sample [26,27], i.e. the deflection δ of the cantilever versus the displacement Z of the AFM piezo actuator, acquired with the optical lever method (top panel) and with the piezoresistive signal (bottom panel). The *laser curve* has a quite low noise (see below); small, not continuous oscillations along the zero line are most likely due to optical interference [26]. The contact line is fairly straight, and the jump-off contact (minimum of the retraction curve in blue) due to the capillary force can be seen very well.

The *piezoresistive curve* shows a considerably higher noise (not clearly visible here, see below). Hence, it is evident that forces smaller than 25 nN (see below) and small differences of the elastic moduli of the sample cannot be measured with the piezoresistive signal. The slope of 39.62 μm/V of the contact line measured through a linear fit agrees very well with the value of 40 μm/V expected from the sensitivity $S = 250$ V/m of the CAN50-2-5 piezoresistive microprobe and the gain of the preamplifier ($G = 100$).

For determining the noise of the microprobe and thereby the minimum detectable tip deflection, deflection-displacement curves were acquired on glass with different velocities and with different dwell times between approach and retraction. Fig. 7 shows an exemplary curve with a dwell time of 600 s and ca. 20 s loading/unloading times. The red and black curves were acquired using the laser and the piezoresistive signals, respectively. The two insets show the 20 times magnified signals along the zero lines (bottom left) and during a part of the dwell time (top right).

For the noise analysis, three regions of the curves should be distinguished: the zero line (no contact between tip and sample), the dwell region (contact between tip and sample), and the contact line (contact between tip and sample during piezo extension). Table 2 shows the noise deflections of the microprobe tip in nanometers, which were determined as standard deviation (σ) and maximum peak-to-peak deflection in the three mentioned intervals, both for the laser and for the piezoresistive signal. Four deflection-displacement curves with different load-dwell-unload times and with maximum deflections of ca. 2.37 μm were analyzed. For comparison, noise values of a commercial AFM cantilever (PPP-NCSTAuD from Nanosensors, 152 μm long, 29 μm wide, 2.7 μm

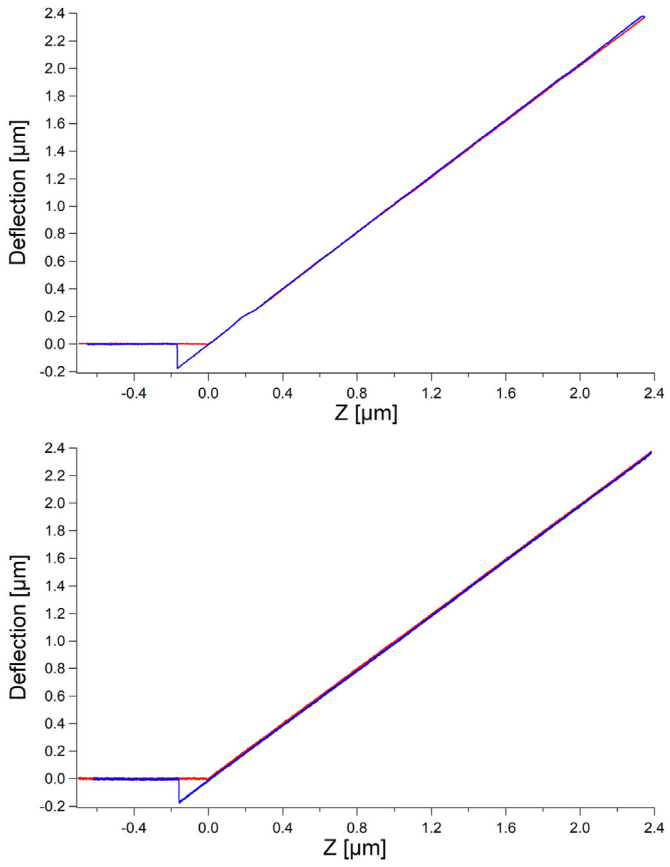

Fig. 6. (Top) Deflection-displacement curve on a glass surface acquired in air with the optical-lever method at a frequency of 0.15 Hz. **(Bottom)** Same as in the top panel but using the piezoresistive output signal of the microprobe. The approach curves are in red, the retraction curves in blue. (For interpretation of the references to colour in this figure legend, the reader is referred to the Web version of this article.)

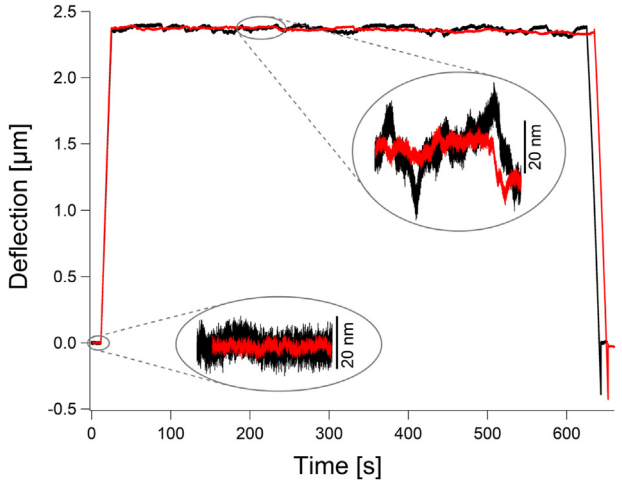

Fig. 7. Deflection curves versus time on a glass surface with a dwell time of ca. 600 s and loading/unloading times of ca. 20 s. The red curve was acquired with the optical lever method, the black one with the piezoresistive signal. The insets show 20 times magnified signals along the zero lines (bottom left) and during a part of the dwell time (top middle). (For interpretation of the references to colour in this figure legend, the reader is referred to the Web version of this article.)

Table 2
Noise deflection in nanometers as standard deviation (σ) and as peak-to-peak noise for four deflection-displacement curves, denoted with the load-dwell-unload times, determined in three different regions of the curves (zero line, loading line, and dwell interval) both for the laser and for the piezoresistive signal. The last three rows show the corresponding noise values measured with a commercial cantilever (PPP-NCSTAuD from Nanosensors, 152 µm long, 29 µm wide, 2.7 µm thick, elastic constant k_c = 7.3 N/m).

		Laser signal		Piezoresistive signal	
		σ	peak-to-peak	σ	peak-to-peak
5-2-5	zero line	1.6	8.9	2.6	17.2
	contact line	1.7	11.6	2.7	19.7
	Dwell	1.5	10	2.7	20.2
10-5-10	zero line	1.3	9.2	2.8	20.9
	contact line	2.1	12.7	2.8	20.2
	Dwell	1.6	11.2	2.9	20.8
20-15-20	zero line	1.1	7.7	2.9	22.1
	contact line	2.6	17.7	3	23.6
	Dwell	1.8	13	3.1	24.3
20-600-20	zero line	1.4	9.5	2.9	21.8
	contact line	2.8	17.5	3.9	27.5
	Dwell	7.5	45.8	18.7	101.9
Theoretical	1000 s zero line			2.4	
	1000 s dwell			3.0	
8-600-8 with PPP-NCSTAuD	zero line	0.02	0.24		
	contact line	0.03	0.18		
	Dwell	0.1	0.76		

thick, elastic constant k_c = 7.3 N/m) in the three regions are given in the last three rows. All curves were smoothed using a low pass filter with a cut-off frequency of 1 kHz. In addition, theoretical noise values were calculated using Eqs. (1) to (5) and the respective data in Table 1 for zero deflection and δ = 2.5 µm, respectively.

In general, the noise is smaller along the zero line, since tip and sample are not in contact and the only sources of noise are the thermal noise of the cantilever and the electronic noise of the optical lever and of the microprobe output signals, respectively. The noise increases when tip and sample are in contact, due to mechanical vibrations of the sample, notably along the contact line, since the piezo is extending. The considerably higher noise during the 600 s dwell is due to long-time oscillations; we find a vertical drift of ca. 40 nm in 600 s for both curves. It should be noted that no feedback signal was used during the dwell. The tip was kept statically in the position where the trigger point was reached.

As can be noted already in Fig. 7, in particular in the left bottom inset, in all three regions, the noise in the curves acquired with the piezoresistive signal is higher (typically twice as high, up to a factor of 2.9) than in the curves acquired with the laser signal.

Since the microprobe used for the measurements is exactly the same, the differences between the noise measured with the piezoresistive signal and the laser signal in Table 2 cannot be due to the mechanical-thermal noise of the cantilever or to vibrations of the sample. They are expected to be caused by differences in the sensitivity of the two signals and the electronic noise caused by the piezoresistive Wheatstone bridge, the instrumentation preamplifier, and fluctuations of the bridge supply voltage. In fact, the measured noise values of the piezoresistive signal agree very well with the theoretical expectation calculated using Eqs. (1) to (5). Furthermore, with small piezoresistive cantilevers of L = 70 µm, w = 30 µm, and b = 4 µm to 6 µm (PRS probes, SCL-Sensor.Tech. Fabrication GmbH, Austria), a sensitivity of $S \approx 0.05$ V/µm and a resolution of $\approx$ 0.03 nm at a bandwidth of Δf = 20 kHz were reported [13], which corresponds well to the noise values observed with the PPP-NCSTAuD in the present study (Table 2).

For dwell times up to 15 s, we do not detect considerable drift of the deflection during the dwell phase. We conclude that the microprobe holder is mechanically stable without any compliant elements, e.g., glued connections between the microprobe die and its PCB and between the microprobe PCB and the aluminum body. For the 600 s dwell, additional noise sources, e. g., due to electromagnetic radiation, which was not considered in our theoretical calculations, or long-time oscillations may have led to the strongly impaired resolution of the piezoresistive microprobe.

The comparison with the commercial AFM cantilever shows that the noise of the microprobe, even with the laser signal, is 1 to 2 orders of magnitude higher. The vertical drift of the commercial cantilever (14 nm in 10 min) is lower, too. The considerably larger noise of the microprobe cannot be explained by the cantilever geometry as in the case of the piezoresistive read-out. In the case of optical-lever read-out, measurement noise must be considered in addition to thermal noise. For the latter we calculate using [27]:

$$\delta_{\mathrm{th}} = \sqrt{c\frac{k_{\mathrm{B}}T}{3k_{\mathrm{c}}}} \tag{7}$$

with $c = 4$ (and $c = 1$), i. e., in the cases without (and with) contact to a (hard) sample, respectively, similar values of $\delta_{\mathrm{th}} = 24.5\ \mathrm{pm_{RMS}}$ ($12.3\ \mathrm{pm_{RMS}}$) and $27.2\ \mathrm{pm_{RMS}}$ ($13.6\ \mathrm{pm_{RMS}}$) for the microprobe ($k_{\mathrm{c}} = 8.45\ \mathrm{N/m}$) and the PPP-NCSTAuD ($k_{\mathrm{c}} = 7.3\ \mathrm{N/m}$).

More than thermal noise, the noise of the optical-lever read-out technique represented by laser and photodiode shot noise and noise by the read-out electronics dominates the total integrated noise. Assuming an optimum design of the optical-lever system, the photodiode shot noise will usually dominate the total integrated noise with a theoretical lower limit of 60 pm at a low-pass filter bandwidth of 10 kHz [28]. While this optimal design of the optical lever system was realized for the PPP-NCSTAuD, considerable optimization (i.e. laser spot size, positioning on the cantilever, increasing the reflectivity of the cantilever) would be necessary for the CAN50-2-5 to yield similar low noise values. In this study, however, we forego and concentrate on evaluating the piezoresistive output performance of the microprobe, for which we experimentally found deflection noise values according to the theoretical expectation.

The microprobe was employed to acquire the topography of a scratched glass surface in contact mode, both with the common laser signal and with the piezoresistive signal, as shown in Fig. 8. The scan area was $(25\ \mu\mathrm{m})^2$ in both cases. Due to the low sensitivity of the piezoresistive signal, in order to get a suitable feedback loop, the corresponding image was acquired at a low frequency (0.1 Hz instead of 1 Hz). The alternative of adjusting the feedback parameters was thoroughly examined. However, a degradation of feature clarity was observed. A future redesign of the interface PCB with the aim of amplifying the piezoresistive signal corresponding to the optical readout should allow to increase the scan frequency to 1 Hz without losing clarity.

The congruence of the two topographies is very high. This confirms that the topography of samples can be detected with high resolution using both the optical-lever and the piezoresistive signal. Some details of the topography are sharper in the *piezoresistive image*, due to the lower scanning frequency.

Several details in the two topographies in Fig. 8 show that – at this stage of the measurements – the tip has a sharp spherical apex with a radius smaller than 200 nm. In the following measurements, due to several contact scans in between, tip wear occurred. Therefore, in the following, the blunt tip should be modeled with a truncated pyramid or a truncated cone, and not with a paraboloid. The width of the apex is between 2 μm and 3 μm. It was not determined before each measurement, in order to avoid further wear.

Fig. 9 shows the results of a force-volume measurement on the edge of an AZ 5214E photoresist film on silicon, acquired by exploiting the piezoresistive signal. A force-volume [25, pp. 79–80] is an array of

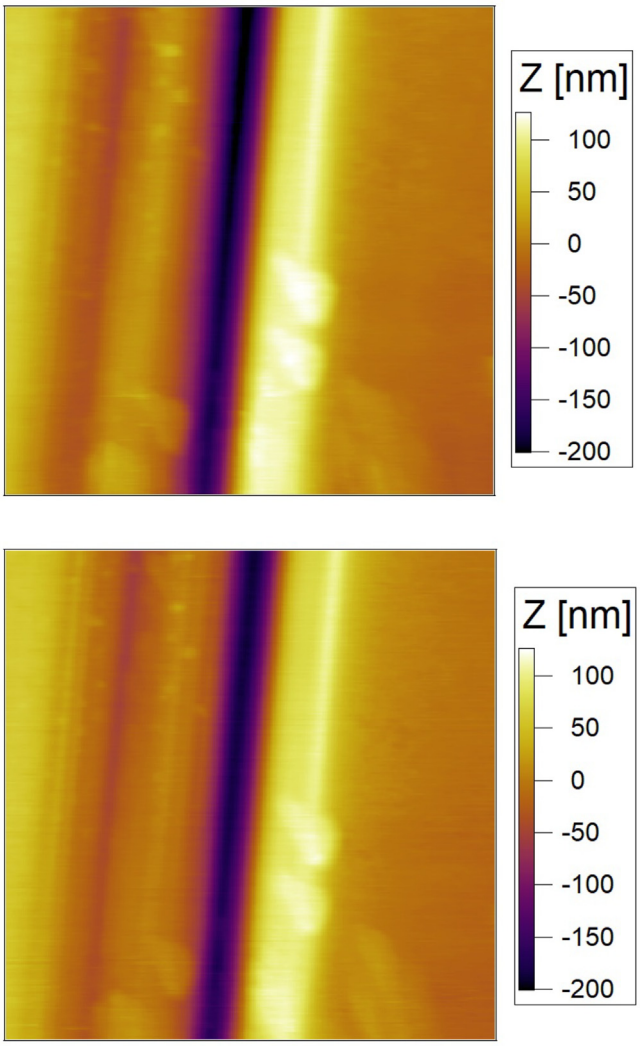

Fig. 8. Topography of a scratched glass surface acquired in air with the optical lever method at a line acquisition rate of 1 Hz **(top)** and with the piezoresistive signal at 0.1 Hz **(bottom)**. Both scan areas are $(25\ \mu\mathrm{m})^2$.

force-distance curves (50×50 in this case) acquired on a certain area ($25 \times 25\ \mu\mathrm{m}^2$) with the same maximum force (10 μN) and the same curve acquisition frequency (1 Hz). The top part of the figure shows two typical deflection-displacement curves on silicon (left) and on the polymer film (right). Approach curves are in red, retraction curves are in blue.

Apart from the high noise in the curves, which has been already discussed, a feature of the retraction curve on silicon is remarkable, namely the oscillations after the jump-off-contact, i.e. the discontinuity separating the zero line and the contact line in the retraction curve. The adhesion is mainly caused by the capillary force exerted by a thin water film on the sample. The oscillations after the jump-off-contact are a consequence of the sudden break of the water meniscus and of the following sudden detachment of the tip from the sample. Due to its low resonance frequency, the CAN50-2-5 oscillates with an exponential damping for ca. 0.14 s after detachment. This artifact, which may result in a serious drawback for the automatic analysis of force-volume measurements, has to be avoided, e. g. by a damping layer on the cantilever.

The bottom part of Fig. 9 shows the topography (left), the stiffness map (middle), and the map of the adhesion force (right). The silicon substrate is on the left side of the maps, the polymer film on the right side. The topography was measured as the value Z_{max}, at which the maximum force is reached. This value is a measure of the local height of the sample only if deformations are small; this is the case in the present

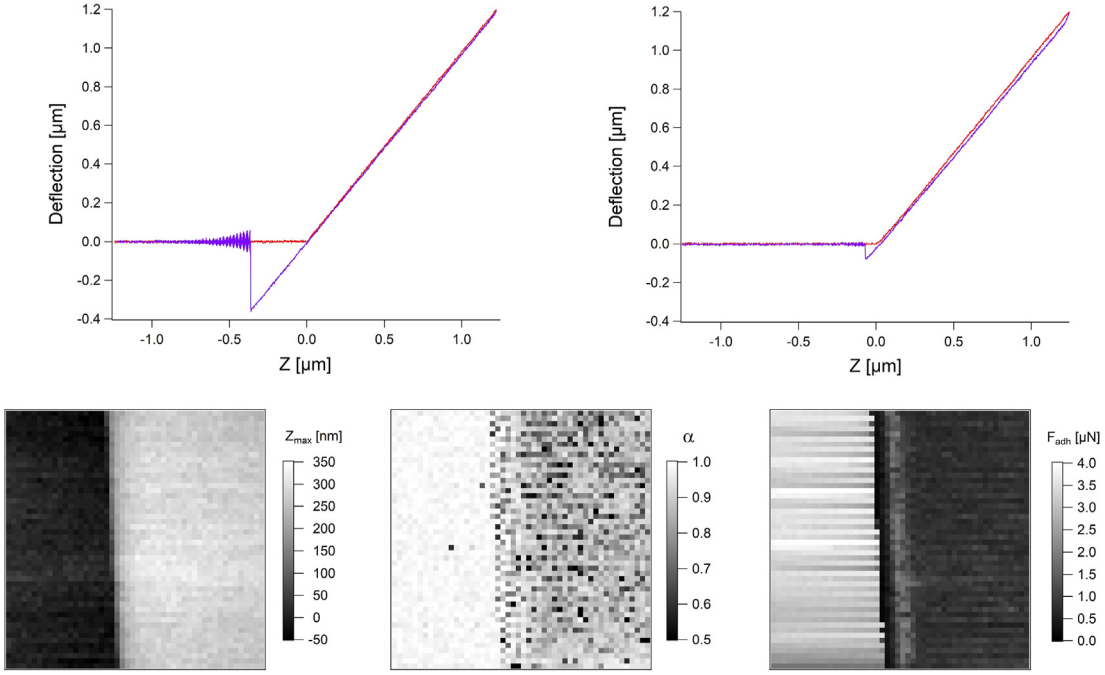

Fig. 9. Force-volume at the border of an AZ 5214E film on silicon, acquired by exploiting the piezoresistive signal. **(Top)** Typical deflection-displacement curves on bare silicon (left) and on AZ 5214E/silicon (right). Approach curves are in red, retraction curves are in blue. **(Bottom)** Topography (left) and maps of the stiffness (middle) and of the adhesion force (right). The area of the maps is $(25\ \mu m)^2$. The silicon substrate is on the left side of the maps, the polymer film on the right side. (For interpretation of the references to colour in this figure legend, the reader is referred to the Web version of this article.)

measurement. Despite the larger noise of the CAN50-2-5 microprobe compared to the AFM cantilever, the bare silicon and polymer-coated areas of the sample can be distinguished very well. The thickness of the polymer film is determined to 279 nm ± 28 nm.

In general, the stiffness of the cantilever-sample system is a rough measure of the mechanical properties of the sample. Along the contact line, the following equation is valid in the limit of small sample deformations [25,29]:

$$k_c\delta = \frac{k_c k_s}{k_c + k_s} Z = k_{eff} Z, \tag{8}$$

where k_c and k_s are the elastic constants of cantilever and sample, modeled as springs. The relative effective contact stiffness is given by $\alpha = k_{eff}/k_c$. If the sample is much stiffer than the cantilever, $k_{eff} \approx k_c$, i.e. $\alpha \approx 1$ and $\delta \approx Z$; at the other limit, if the sample is much more compliant than the cantilever, $k_{eff} \approx k_s$ and $\alpha \approx 0$. This model is quite simplistic; as a matter of fact, the sample cannot be described as a spring and its "spring constant" depends on the contact area. Following Hertz theory, the "spring constant" of the sample is given by:

$$k_s = \frac{3}{2}\sqrt[3]{FRE_{tot}^2}, \tag{9}$$

where R is the tip radius and the reduced elastic modulus E_{tot} is yielded by:

$$\frac{1}{E_{tot}} = \frac{3}{4}\left(\frac{1-\nu^2}{E} + \frac{1-\nu_t^2}{E_t}\right), \tag{10}$$

with E and E_t and ν and ν_t denoting Young's moduli and Poisson's ratios of sample and AFM tip, respectively. Equation (9) is valid for a hemispherical or paraboloidal tip. Also for other tip geometries, even if different exponents must be used, k_s depends on the geometrical parameters describing the tip.

Even a simple observation of the typical force-distance curves in the upper row of Fig. 9 shows that deformations of the polymer film, and hence differences in the stiffness, occur only at the beginning of the contact. Hence, in order to enhance the contrast in the map, the stiffness was calculated by fitting a short part of the approach curve after the jump-to-contact ($0 < Z < 130$ nm). This contrast is not very pronounced, since the used tip of the CAN50-2-5 was large and therefore $k_{eff} \approx k_c$ not only on the bare silicon but also on the polymer film. With $k_c = 8$ N/m, $R = 1$ µm, and $F = 5$ µN, a sample with $E_{tot} = 0.18$ GPa is already 10 times stiffer than the cantilever. Nevertheless, the two regions of the sample can be distinguished. The values of the stiffness on silicon and on AZ 5214E are 0.98 ± 0.02 and 0.90 ± 0.08, respectively.

The adhesion force F_{adh} was measured as the force at the jump-off-contact. The values on silicon and on AZ 5214E are 3.3 µN ± 0.5 µN and 0.77 µN ± 0.18 µN, respectively. The distinct contrast in the adhesion map is due to the strong interaction between the silicon sample and the silicon tip, the large tip radius, and the roughness of the polymer film, reducing the contact area with the tip. Furthermore, since adhesion in air is mostly due to the capillary forces exerted by a thin water layer adsorbed on the sample surface, it can be assumed that AZ 5214E is less hydrophilic than silicon; hence the water layer adsorbed on it is thinner and exerts a lower force. The very low adhesion at the very edge of the polymer film is due to topography artifacts, which affect the contact area, too [25, pp. 83–85]. Instead, stripes on the silicon surface, visible only in the adhesion map, are a consequence of tip contamination with polymer, depending on the scan direction.

On a similar sample (same polymer on silicon, but with a lower thickness), measurements were performed in Dual AC Resonance Tracking (DART) mode [30,31] exploiting the piezoresistive signal. In DART mode, while scanning the sample in contact at a certain load, the cantilever is excited at two frequencies on either side of its contact resonance frequency f_c. This allows the tracking of f_c.

Fig. 10 shows four maps obtained through a DART-measurement on a 30 µm × 28.115 µm area at the border of the polymer-coated region. The bare silicon substrate is on the left side of the maps, the polymer film on the right side. The measurement was performed with a static load of 6.8 µN exploiting the first flexural mode. In the top panel, the topography

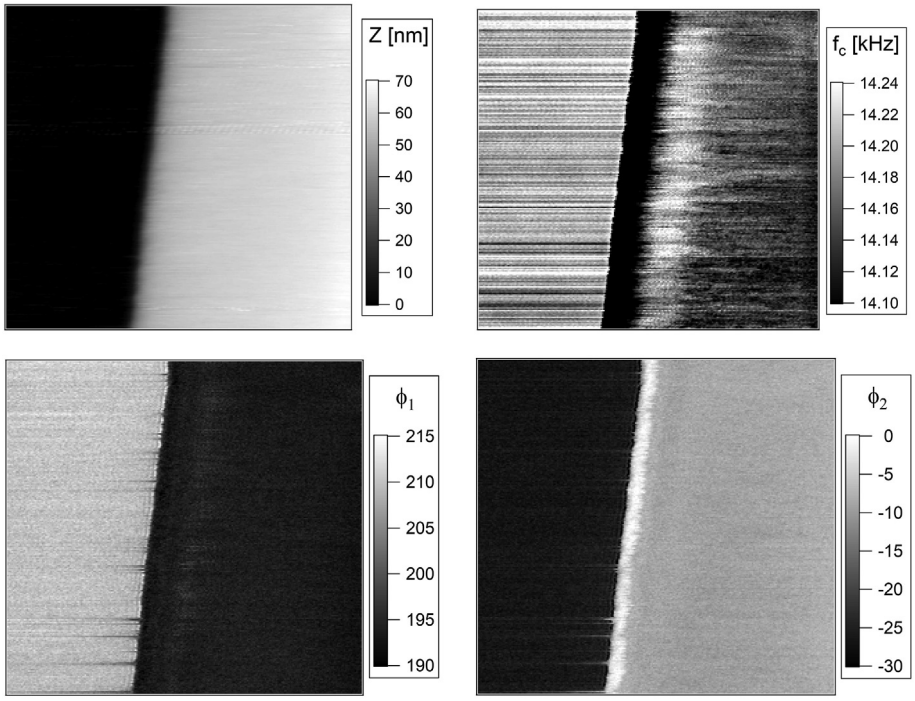

Fig. 10. DART-measurement at the border of an AZ 5214E film on silicon, acquired by exploiting the piezoresistive signal. **(Top)** Topography (left) and contact resonance frequency (right). **(Bottom)** Phase shift of the oscillation corresponding to both frequencies on either side of the contact resonance frequency. The area of the maps is $30 \cdot \mu m \times 28.115 \cdot \mu m$. The bare silicon is on the left side of the maps, the polymer film on the right side.

(left) and the contact resonance frequency (right) are shown. The bottom panel displays the phase shift of the oscillation corresponding to both frequencies on either side of the contact resonance frequency.

The topography map shows that the edge of the polymer film is 51 nm ± 2 nm high and ca. 2.6 μm wide. Yet, the width is affected by the large radius of the tip of the CAN50-2-5. Furthermore, the thickness of the film increases with the distance from the edge (ca. 0.8 nm per micrometer).

The contact resonance frequency f_c depends on the elastic modulus E of the sample, and hence on sample stiffness. In particular, f_c increases with increasing modulus [32]. If the system can be modeled as two springs with elastic constants k_c (cantilever) and k_s (sample) and deformations are only elastic and can be described by Hertz theory (i.e., the adhesion is negligible), the contact resonance frequency can be written as [33]:

$$f_c \approx \left[\frac{5}{4}\pi\frac{1}{\gamma x_0 L}\left(1-\left(\frac{5}{12}\pi\right)^2\frac{k_c}{\sqrt[3]{FRE_{tot}^2}}\right)\right]^2 f_0 = \left[\frac{5}{4}\pi\frac{1}{\gamma x_0 L}\left(1-\frac{1}{6}\left(\frac{5}{4}\pi\right)^2\frac{k_c}{k_s}\right)\right]^2 f_0. \quad (11)$$

The parameter γ is the relative position of the tip on the cantilever; $x_0 L$ and f_0 are the wavenumber and the free resonance frequency for the first free flexural mode.

The contrast in the frequency map between the bare silicon and the polymer-coated areas is not very pronounced. This is due to the small differences in modulus between substrate and a thin film, but also to the large tip radius, which increases k_s. The large tip radius and the presence of a sharp step in the topography, reducing the contact area, are responsible also for the very low contact resonance frequencies at the very edge of the polymer film. Nevertheless, in the histogram of the contact resonance frequency plotted in Fig. 11, the two materials in the two regions of the sample can be distinguished.

The histogram was fitted with a double Gauss curve; the contribution of the polymer-coated silicon is centered at 14.145 kHz with a width of 35 Hz, the contribution of the bare silicon is centered at 14.200 kHz with

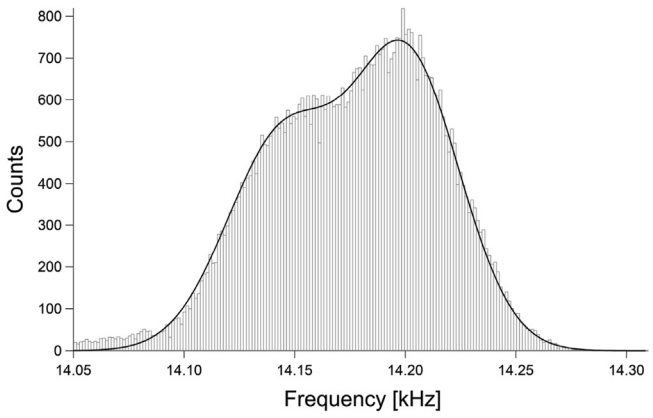

Fig. 11. Histogram of the contact resonance frequency fitted with a double Gauss curve.

a width of 34 Hz. This is in good agreement with previous measurements using CAN50-2-5 sensors and AZ 5214 samples, where we measured contact resonance frequencies in the range of 14.11 kHz to 14.27 kHz with standard deviations of 21 Hz to 41 Hz [8]. Furthermore, studies with other thin polymer films on silicon substrates using these sensors report similar frequencies [6,9,34]. A better signal-to-noise ratio can be expected using higher resonance modes, e. g. the second mode as shown in Ref. [8]. However, a higher probing force will then be necessary to offset the lower deflection amplitude.

It is difficult to name the exact origin of the fluctuations of the contact resonance frequency that are visible in Fig. 10. In this measurement, they probably originated from contamination of the tip with polymer particles. This contamination could have happened when the tip was scanned across the polymer film. Most likely, the contaminants got lost later during the scan. Nevertheless, the fluctuations were in a very narrow frequency interval. This can be seen in the histogram in Fig. 11, where the peaks corresponding to the bare silicon and the

polymer-coated silicon can be clearly distinguished, although they differ by only 55 Hz.

A quantitative analysis using Equation (11) appears to be rather speculative due to the non-ideal shape of the tip and its unknown relative position γ, which has a sensitive effect on the contact stiffness. Regarding the large uncertainties, which have to be expected, and the limited amount of experimental data obtained so far, quantitative results for contact stiffness or tip radius might be considered as rather meaningless and shall thus not be given here.

The two maps of the phase shift corresponding to the selected frequencies on either side of the contact resonance show a very clear contrast between silicon and AZ 5214E. The phase shift is related to energy dissipation but cannot be easily modeled. The large differences in the adhesion are likely to be responsible for the differences in phase shift.

Another application of a force volume is the characterization of a thin lubricant film on a substrate [35,36]. Due to its dimensions and versatile read-out, the CAN50-2-5 piezoresistive microprobe is an excellent choice for such a task, e.g. on non-planar workpieces. Here, as an exemplary application, a force volume was acquired on a glass surface covered with a liquid lubricant, namely Lupranol VP 9209 (BASF, Germany), a polyalkylene glycol.

A single deflection-displacement curve is plotted in Fig. 12, with the approach part in black and the retraction part in gray [37,38]. At a distance of 174 nm from the glass substrate, the tip jumps into contact with the liquid. Afterwards, the tip goes through the liquid film, which wets the tip, leading to a slightly attractive force, till the tip comes into contact with the glass substrate and the force becomes repulsive. In the retraction curve, the detachment from the liquid takes place at a distance of 2516 nm, which is much larger than the thickness of the Lupranol layer. For this lubricant, this is due to the formation of a meniscus and to the (partial) pinning of the three-phase contact line. Hence, the meniscus is stretched before the liquid detaches from the tip.

Such curves can be used to detect the thickness t of a liquid film on an arbitrary body. It is given as the distance between the jump-to-contact with the liquid and the jump-to-contact with the substrate, minus the deflection of the cantilever at the jump-to contact with the substrate. The thickness can be mapped, as shown in the top panel of Fig. 13.

The map shows a liquid film with an average thickness of 90 nm in the bottom right corner of the scanned surface. As can be seen in the line profile in the bottom panel, although the distance between two successive curves (600 nm) is smaller than the width of the apex of the truncated tip, the borders of the liquid film can be detected quite well. At some points on the bare substrate small drops with a thickness of ca. 20 nm are visible. This is due to the noise in the deflection-displacement curves, affecting the automatic analysis, and/or to the presence of small lubricant droplets on the tip.

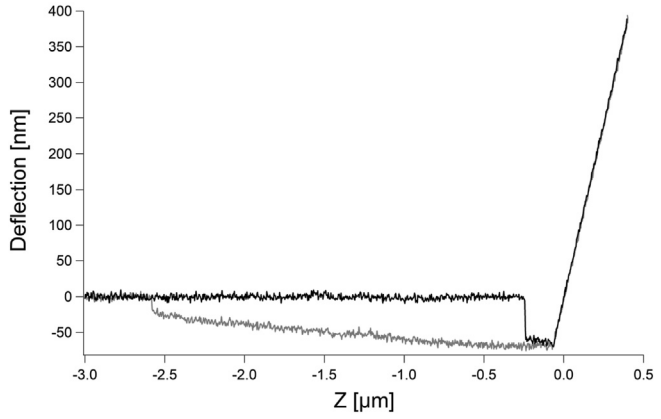

Fig. 12. Deflection-displacement curve on a Lupranol film on glass surface acquired with the piezoresistive signal of the microprobe at 1 Hz. The approach curve is in black, the retraction curve in gray.

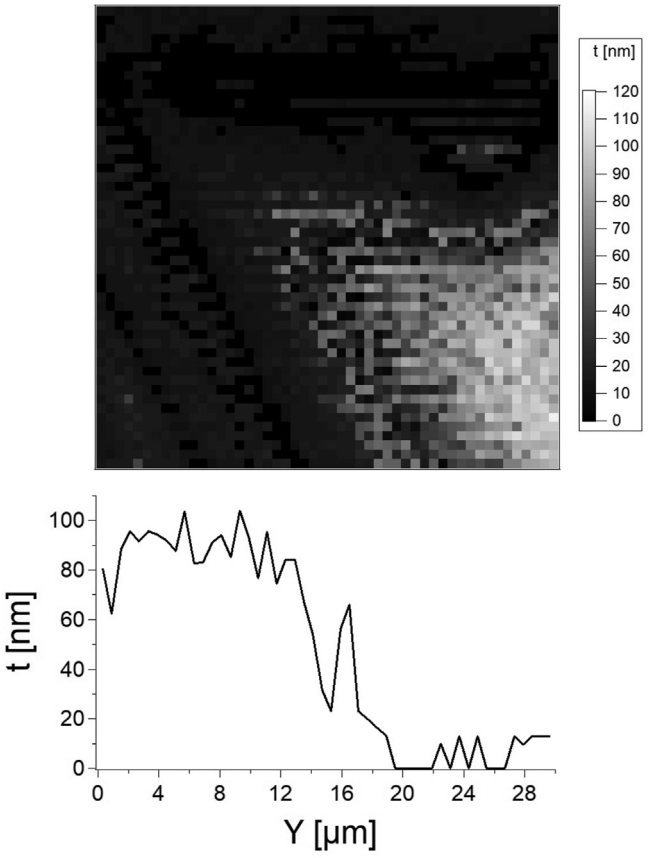

Fig. 13. (Top) Map of the thickness of a Lupranol liquid film partially covering a glass surface, with 50 × 50 deflection-displacement curves over an area of $(30\ \mu m)^2$. **(Bottom)** Vertical line profile across the thickness map at the horizontal position $x = 27.8\ \mu m$. The origin of the coordinate system is in the lower left corner of the thickness map.

5. Conclusion

A long slender piezoresistive silicon microprobe (CAN50-2-5, CiS Forschungsinstitut für Mikrosensorik, Erfurt, Germany) with customized dimensions aimed for versatile metrological tasks on industrial work pieces was investigated in a Cypher atomic force microscope (AFM) and compared to standard AFM probes as a benchmark. For this, a probe holder was designed and fabricated which enabled a drop-in replacement of the standard cantilever holder without requiring to adapt in the AFM itself. Deflection-displacement curves on glass using the piezoresistive output signal revealed a vertical resolution of 2.8 nm at a bandwidth of 1 kHz, which corresponds well to the theoretical value of 3.0 nm expected from sensitivity and noise of the microprobe. With area-selectively thin polymer-coated silicon wafers, force-volume and contact-resonance measurements were performed yielding maps of topography, stiffness and adhesion force with reasonable contrast across the different areas of the samples. Lateral resolution was found to be limited by the diameter of the apex area of the silicon probing tip (of few µm), which was affected by wear and thus took the shape of a truncated pyramid or cone similar to Refs. [3,6]. Nevertheless, using force-volume measurements with liquid samples, a thickness map of a 90 nm lubricant layer on silicon could be obtained. In this case the lateral resolution was sufficient to reveal the lateral limitation of the liquid film reasonably.

These results confirm that the piezoresistive silicon microprobe is a promising candidate to solve various emerging tasks of industrial surface metrology, e. g. fast micro-finish measurements on manufacturing machines, including flatness, waviness, roughness and microform as well as elasticity, thickness, adhesion, wear, etc. of thin solid or liquid deposits

on work pieces. Increase of the measurement range, higher damping for high-speed scanning and direct cantilever actuation for high-order-mode contact-resonance spectroscopy are the next steps of improvements of the microprobe features. Furthermore, the present silicon tips will be replaced by glued diamond tips to ensure stable well-defined contact conditions.

Data availability statement

All figures and raw data have been published in Zenodo (https://doi.org/10.5281/ZENODO.4610489).

CRediT authorship contribution statement

Michael Fahrbach: Conceptualization, Formal analysis, Writing – original draft, Visualization. **Sebastian Friedrich:** Resources, Writing – original draft, Investigation. **Heinrich Behle:** Resources. **Min Xu:** Investigation. **Brunero Cappella:** Conceptualization, Formal analysis, Writing – original draft, Supervision. **Uwe Brand:** Validation, Writing – review & editing, Project administration. **Erwin Peiner:** Conceptualization, Writing – original draft, Supervision.

Declaration of competing interest

The authors declare that they have no known competing financial interests or personal relationships that could have appeared to influence the work reported in this paper.

Acknowledgments

This project 17IND05 MicroProbes has received funding from the EMPIR programme co-financed by the Participating States and from the European Union's Horizon 2020 research and innovation programme.

We acknowledge support by the German Research Foundation and the Open Access Publication Funds of Technische Universität Braunschweig.

References

[1] E. Peiner, M. Balke, L. Doering, Form measurement inside fuel injector nozzle spray holes, Microelectron. Eng. 86 (4–6) (2009) 984–986, https://doi.org/10.1016/j.mee.2008.12.016.

[2] E. Peiner, L. Doering, Nondestructive evaluation of diesel spray holes using piezoresistive sensors, IEEE Sensor. J. 13 (2) (2013) 701–708, https://doi.org/10.1109/jsen.2012.2225614.

[3] T. Frank, L. Doering, G. Heinrich, N. Thronicke, C. Löbner, S. Völlmeke, A. Steinke, S. Reich, Silicon cantilevers with piezo-resistive measuring bridge for tactile line measurement, Microsyst. Technol. 20 (4–5) (2014) 927–931, https://doi.org/10.1007/s00542-014-2092-0.

[4] CiS Forschungsinstitut für Mikrosensorik GmbH, Piezoresistive mikrotaster, URL, https://www.cismst.de/fileadmin/user_upload/publikationen/cantilever.pdf, 2014.

[5] L. Doering, U. Brand, S. Bütefisch, T. Ahbe, T. Weimann, E. Peiner, T. Frank, High-speed microprobe for roughness measurements in high-aspect-ratio microstructures, Meas. Sci. Technol. 28 (2017), https://doi.org/10.1088/1361-6501/28/3/034009.

[6] U. Brand, M. Xu, L. Doering, J. Langfahl-Klabes, H. Behle, S. Bütefisch, T. Ahbe, E. Peiner, S. Völlmeke, T. Frank, B. Mickan, I. Kiselev, M. Hauptmannl, M. Drexel, Long slender piezo-resistive silicon microprobes for fast measurements of roughness and mechanical properties inside micro-holes with diameters below 100 μm, Sensors 19 (6) (2019) 1410, https://doi.org/10.3390/s19061410.

[7] Physikalisch-Technische Bundesanstalt, 17ind05 microprobes multifuntional ultrafast microprobes for on-the-machine measurements, URL, https://www.ptb.de/empir2018/microprobes/.

[8] M. Bertke, M. Fahrbach, G. Hamdana, J. Xu, H.S. Wasisto, E. Peiner, Contact resonance spectroscopy for on-the-machine manufactory monitoring, Sensor Actuator Phys. 279 (2018) 501–508, https://doi.org/10.1016/j.sna.2018.06.012.

[9] M. Fahrbach, S. Friedrich, B. Cappella, E. Peiner, Calibrating a high-speed contact-resonance profilometer, Journal of Sensors and Sensor Systems 9 (2) (2020) 179–187, https://doi.org/10.5194/jsss-9-179-2020. URL, https://jsss.copernicus.org/articles/9/179/2020/.

[10] M. Xu, J. Kirchhoff, U. Brand, Development of a traceable profilometer for high-aspect-ratio microstructures metrology, Surf. Topogr. Metrol. Prop. 2 (2) (2014), 024002, https://doi.org/10.1088/2051-672x/2/2/024002.

[11] M. Xu, F. Kauth, B. Mickan, U. Brand, Traceable profile and roughness measurements inside micro sonic nozzles with the profilscanner, in: B. Larquier (Ed.), 17th International Congress of Metrology, EDP Sciences, 2015, https://doi.org/10.1051/metrology/20150013004.

[12] M. Xu, F. Kauth, B. Mickan, U. Brand, Traceable profile and roughness measurements inside small sonic nozzles with the profilscanner to analyse the influence of inner topography on the flow rate characters, Meas. Sci. Technol. 27 (9) (2016), 094001, https://doi.org/10.1088/0957-0233/27/9/094001.

[13] M. Dukic, J.D. Adams, G.E. Fantner, Piezoresistive AFM cantilevers surpassing standard optical beam deflection in low noise topography imaging, Sci. Rep. 5 (1) (2015), https://doi.org/10.1038/srep16393. Nov.

[14] E. Peiner, L. Doering, M. Balke, A. Christ, Silicon cantilever sensor for micro-/nanoscale dimension and force metrology, Microsyst. Technol. 14 (4–5) (2007) 441–451, https://doi.org/10.1007/s00542-007-0436-8.

[15] E. Peiner, M. Balke, L. Doering, Slender tactile sensor for contour and roughness measurements within deep and narrow holes, IEEE Sensor. J. 8 (12) (2008) 1960–1967, https://doi.org/10.1109/jsen.2008.2006701.

[16] T.B. Gabrielson, Mechanical-thermal noise in micromachined acoustic and vibration sensors, IEEE Trans. Electron. Dev. 40 (5) (1993) 903–909, https://doi.org/10.1109/16.210197.

[17] J.C. Doll, B.L. Pruitt, Piezoresistor design and applications, in: Of Microsystems and Nanosystems, vol. 1, Springer, New York, 2013, https://doi.org/10.1007/978-1-4614-8517-9.

[18] M.A. Hopcroft, W.D. Nix, T.W. Kenny, What is the young's modulus of silicon? Journal of Microelectromechanical Systems 19 (2) (2010) 229–238, https://doi.org/10.1109/jmems.2009.2039697.

[19] U. Rabe, Atomic force acoustic microscopy, in: B. Bhushan, H. Fuchs (Eds.), Applied Scanning Probe Methods II, Springer Berlin Heidelberg, 2006, pp. 37–90, https://doi.org/10.1007/3-540-27453-7_2.

[20] G. Hamdana, Mems Piezoresistive Force Sensors Based on Micro-/nanostructured Silicon Components, phdthesis, Technische Universität Braunschweig, München, 2018. URL, https://www.dr.hut-verlag.de/9783843938853.html.

[21] K. Achtenberg, J. Mikołajczyk, C. Ciofi, G. Scandurra, Z. Bielecki, Low-noise programmable voltage source, Electronics 9 (8) (2020) 1245, https://doi.org/10.3390/electronics9081245.

[22] LT3045: 20V, 500mA, Ultralow Noise, Ultrahigh PSRR Linear Regulator, Analog Devices Inc., 2019. URL, B. https://www.analog.com/media/en/technical-documentation/data-sheets/LT3045.pdf. (Accessed 16 March 2021).

[23] AD8421: 3 nV/$\sqrt{}$Hz, Low Power Instrumentation Amplifier, Analog Devices, Inc, 2020. URL, A. https://www.analog.com/media/en/technical-documentation/data-sheets/AD8421.pdf. (Accessed 16 March 2021).

[24] LT6657: 1.5ppm/°C Drift, Low Noise, Buffered Reference, Linear Technology Corporation, 2017. URL, D. https://www.analog.com/media/en/technical-documentation/data-sheets/6657fd.pdf. (Accessed 16 March 2021).

[25] B. Cappella, Mechanical Properties of Polymers Measured through AFM Force-Distance Curves, Springer International Publishing, 2016, https://doi.org/10.1007/978-3-319-29459-9.

[26] B. Cappella, G. Dietler, Force-distance curves by atomic force microscopy, Surf. Sci. Rep. 34 (1–3) (1999) 1–104, https://doi.org/10.1016/s0167-5729(99)00003-5.

[27] H.-J. Butt, M. Jaschke, Calculation of thermal noise in atomic force microscopy, Nanotechnology 6 (1) (1995) 1–7, https://doi.org/10.1088/0957-4484/6/1/001.

[28] M.G. Ruppert, N.J. Bartlett, Y.K. Yong, A.J. Fleming, Amplitude noise spectrum of a lock-in amplifier: application to microcantilever noise measurements, Sensor Actuator Phys. 312 (2020) 112092, https://doi.org/10.1016/j.sna.2020.112092.

[29] E. Bonaccurso, B. Cappella, K. Graf, Local mechanical properties of plasma treated polystyrene surfaces, J. Phys. Chem. B 110 (36) (2006) 17918–17924, https://doi.org/10.1021/jp062602w.

[30] B.J. Rodriguez, C. Callahan, S.V. Kalinin, R. Proksch, Dual-frequency resonance-tracking atomic force microscopy, Nanotechnology 18 (47) (2007) 475504, https://doi.org/10.1088/0957-4484/18/47/475504.

[31] A. Gannepalli, D.G. Yablon, A.H. Tsou, R. Proksch, Mapping nanoscale elasticity and dissipation using dual frequency contact resonance AFM, Nanotechnology 22 (35) (2011) 355705, https://doi.org/10.1088/0957-4484/22/35/355705.

[32] D.C. Hurley, J.P. Killgore, Dynamic contact AFM methods for nanomechanical properties, in: Scanning Probe Microscopy in Industrial Applications: Nanomechanical Characterization, John Wiley & Sons, Inc, 2013, pp. 115–149, https://doi.org/10.1002/9781118723111.ch5.

[33] S. Friedrich, B. Cappella, Application of contact-resonance AFM methods to polymer samples, Beilstein J. Nanotechnol. 11 (2020) 1714–1727, https://doi.org/10.3762/bjnano.11.154.

[34] M. Fahrbach, S. Friedrich, B. Cappella, E. Peiner, Calibrating a High-Speed Contact-Resonance Profilometer (Data), 2021, https://doi.org/10.5281/ZENODO.4479804. Jan.

[35] C.M. Mate, M.R. Lorenz, V.J. Novotny, Atomic force microscopy of polymeric liquid films, J. Chem. Phys. 90 (12) (1989) 7550–7555, https://doi.org/10.1063/1.456188.

[36] C.M. Mate, V.J. Novotny, Molecular conformation and disjoining pressure of polymeric liquid films, J. Chem. Phys. 94 (12) (1991) 8420–8427, https://doi.org/10.1063/1.460075.

[37] B. Cappella, Force-distance curves on lubricant films: an approach to the characterization of the shape of the AFM tip, Micron 93 (2017) 20–28, https://doi.org/10.1016/j.micron.2016.11.006.

[38] S. Friedrich, B. Cappella, Study of micro- and nanoscale wetting properties of lubricants using AFM force–distance curves, Tribol. Lett. 68 (1) (2020), https://doi.org/10.1007/s11249-020-1275-3. Feb.